An Ultrafast Shakedown Reveals the Energy Landscape, Relaxation Dynamics, and Concentration of the N_3VH^0 Defect in Diamond

Daniel J. L. Coxon, Michael Staniforth, Ben G. Breeze, Simon E. Greenough, Jonathan P. Goss, Maurizio Monti, James Lloyd-Hughes,* Vasilios G. Stavros,* and Mark E. Newton*

ACCESS | Metrics & More | Article Recommendations | Supporting Information

ABSTRACT: Atomic-scale defects can control the exploitable optoelectronic performance of crystalline materials, and several point defects in diamond are emerging functional components for a range of quantum technologies. Nitrogen and hydrogen are common impurities incorporated into diamond, and there is a family of defects that includes both. The N_3VH^0 defect is a lattice vacancy where three nearest neighbor carbon atoms are replaced with nitrogen atoms and a hydrogen is bonded to the remaining carbon. It is regularly observed in natural and high-temperature annealed synthetic diamond and gives rise to prominent absorption features in the mid-infrared. Here, we combine time- and spectrally resolved infrared absorption spectroscopy to yield unprecedented insight into the N_3VH^0 defect's vibrational dynamics following infrared excitation of the C−H stretch. In doing so, we gain fundamental information about the energies of quantized vibrational states and corroborate our results with theory. We map out, for the first time, energy relaxation pathways, which include multiphonon relaxation processes and anharmonic coupling to the C−H bend mode. These advances provide new routes to quantify and probe atomic-scale defects.
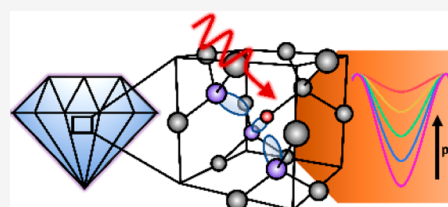
While the uncontrolled incorporation of impurities and defects can limit the functional properties of crystals such as diamond, new opportunities arise when the material is controllably doped. This is exemplified by the exploitation of the optical and spin properties of the negatively charged nitrogen vacancy center (NV^-) in diamond in quantum computing, simulation, and sensing applications.[1−3] Nitrogen is a ubiquitous impurity in both synthetic and natural diamond,[4] with most (∼98%) natural diamonds (classified as type Ia) typically containing 100−1000 ppm nitrogen. In diamond grown by high pressure high temperature (HPHT) or chemical vapor deposition (CVD) synthesis, the concentration of nitrogen can be controlled with less than 1 ppb in the highest purity material.[5] Hydrogen is also a common impurity, and its ability to interact with intrinsic defects,[6] impurities,[7] and surfaces[8] to change electronic and/or optical properties means that it continues to attract considerable attention. Hydrogen is known to interact readily with defects with dangling bonds; for example, with the addition of hydrogen, $NV^{0/-}$ is converted into the stable nitrogen-vacancy-hydrogen ($NVH^{0/-}$) defect.[9,10] Thus, it is of crucial importance that the quantity of hydrogen present in synthetic diamond can be quantified and controlled.

In this letter, we report that time- and energy-resolved infrared absorption spectroscopy can access the potential energy landscape of atomic scale defects and can determine the rate of vibrational coupling to their surroundings. We specifically focus on the 3107 cm^{-1} C−H local vibrational mode (LVM) of the N_3VH^0 defect in diamond, shown in Figure 1a, which consists of a neutral vacancy where three

nearest neighbor carbon atoms have been replaced with nitrogen and a hydrogen is bonded to the remaining carbon neighbor.[4] N_3VH^0 has C_{3V} symmetry, is charge neutral (there is no negatively charged acceptor state version of this defect as all molecular orbitals are full), and has zero spin. The ultrafast "shakedown" of this defect's vibrational dynamics following infrared excitation of the C−H stretch mode ($\nu_S = 3107$ cm^{-1}) provides information about the energies of quantized vibrational states and allows mapping out of the energy relaxation pathways, which include multiphonon relaxation and anharmonic coupling to the C−H bend mode ($\nu_B = 1405$ cm^{-1}). Further, employment of this method offers a new route to quantification of impurities (in this case both nitrogen and hydrogen) incorporated into infrared active defects, which is vital to the characterization of diamond and feeds back into an understanding of synthesis, response to treatments, and impurity incorporation.

There are a number of reasons why N_3VH^0 was chosen for this study. It is common in natural type Ia diamond, where the intensity of the C−H stretch mode can exceed the intrinsic multiphonon absorption in so-called "hydrogen-rich" diamonds. Traditional models for diamond formation within the
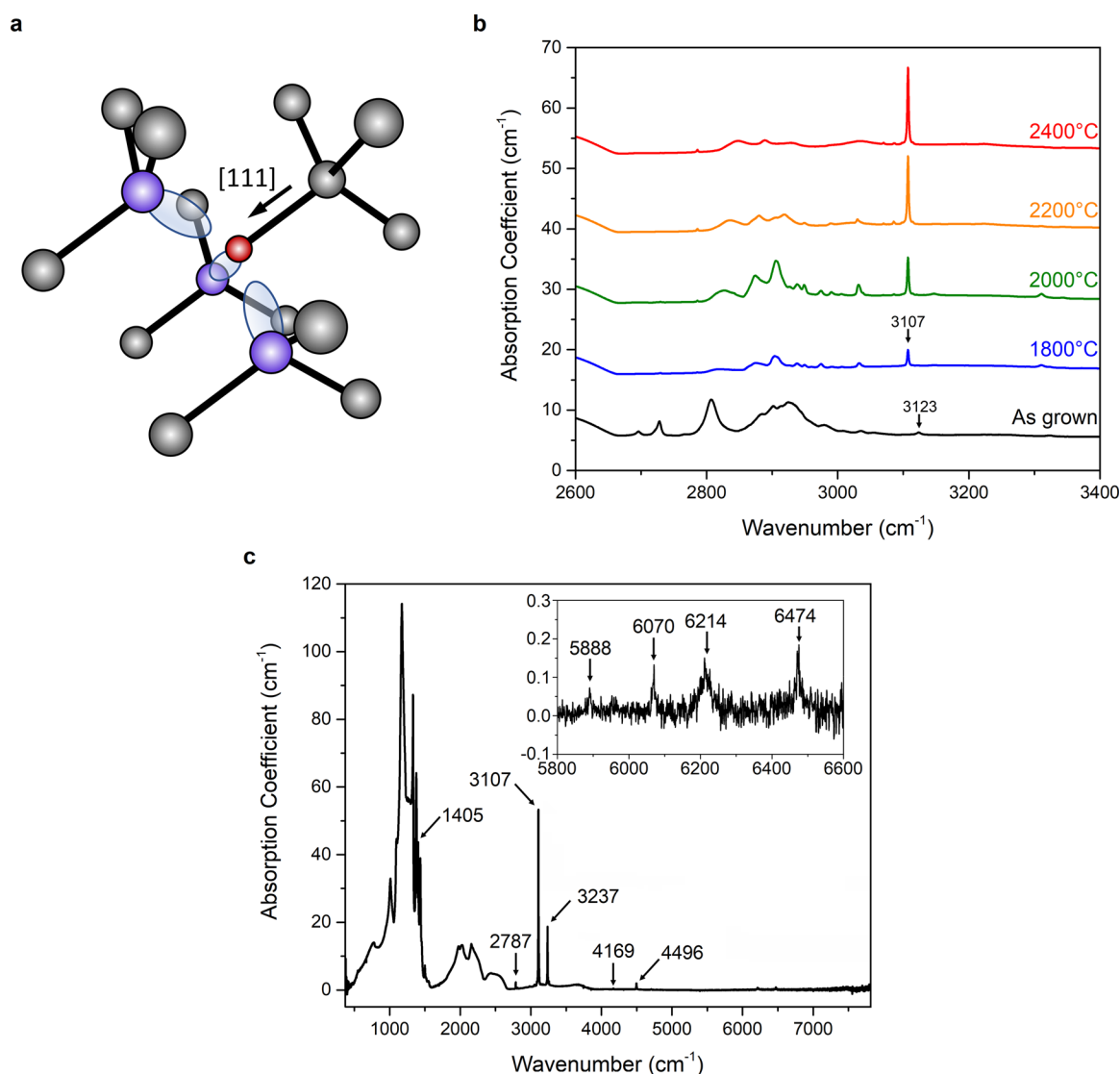
Figure 1. Structure and IR absorption of N_3VH^0 defect. (a) The C−H stretch is along the [111] direction. Gray, blue, and red spheres represent C, N, and H atoms, respectively. (b) Infrared spectra of the C−H stretch region for a suite of CVD grown samples, from which sample S1 (annealed at 2200 °C) was taken. Each sample was subjected to 30 min of high-temperature annealing, at a pressure of 6.6 GPa. Spectra were taken at room temperature and are offset for clarity. (c) Absorbance spectrum of N1, a hydrogen-rich natural diamond. Peaks at 6214 and 6474 cm^{-1} (double 3107 and 3237 cm^{-1}) correspond to photons that interacted with two defects in sequence. 3237 cm^{-1} is not associated with N_3VH^0.

lithospheric mantle of the earth invoke either carbonate reduction or methane oxidation, but new work suggests diamonds may form through isochemical cooling of H_2O-rich Carbon−Hydrogen−Oxygen fluids.[11] Thus, the incorporation of hydrogen (and other impurities) in natural diamond is of considerable interest. N_3VH^0 can also be produced in nitrogen doped lab-grown diamond by HPHT annealing,[12,13] even in material where no C−H stretch absorption was observed prior to annealing. Due to the strength of its absorption features, N_3VH^0 has already been studied in great detail in the frequency domain,[14−23] which probes the time-averaged optical response. However, very little is known about the time scales or mechanisms for relaxation of its associated LVMs (or for that matter any other hydrogen related vibration in diamond). Such information is vitally important since the excited vibrational states are involved in the dissociation of the C−H bond.

While the lifetimes of vibrational modes in hydrogen defects in silicon have been extracted using ultrafast infrared techniques,[24−26] there are no comparable studies of diamond. Previously, Ulbricht et al. indirectly measured the vibrational relaxation time of the NV$^-$ center, by studying the dynamics of the vibronic excitations using ultrafast spectroscopy in the visible range.[27] However, they could not uniquely identify the origin of the fast vibrational relaxation time reported (<60 fs). Therefore, very little is currently known in general regarding the vibrational dynamics of defects in diamond, or in particular how passivating the NV$^-$ defect with hydrogen alters its LVMs. Furthermore, N_3VH^0 is very stable and appears to be the end product of the defect aggregation process in nitrogen doped diamond grown by CVD. N_3VH^0 may account for a substantial fraction of the total incorporated nitrogen and hydrogen in HPHT-annealed CVD diamond, and thus its quantification is important for determining both the nitrogen and hydrogen concentrations in such material.

Here we report studies on two natural diamond samples (N1 and N2), and a CVD grown sample (S1) that was HPHT annealed at 2200 °C. Figure 1b illustrates the production of
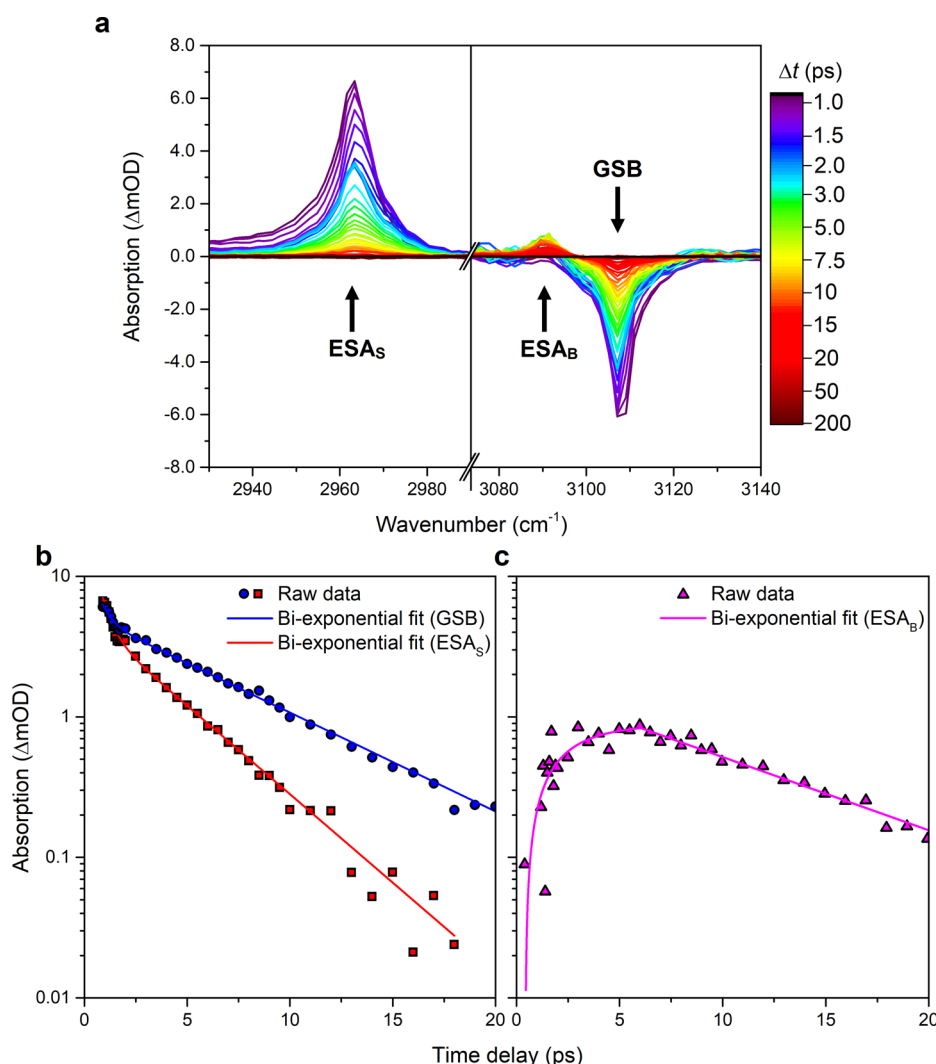
Figure 2. TVAS results for natural diamond N1. (a) Transient absorption spectra for pump−probe delays 1 ps < Δt < 200 ps, for pump excitation centered at 3107 cm^{-1} and probed either around 2960 cm^{-1} (left) or 3107 cm^{-1} (right). (b) Absorption change |ΔA| for GSB (blue circles), ESA$_S$ (red squares) at their maxima, and biexponential fits (solid lines). (c) Absorption change |ΔA| for ESA$_B$ (magenta triangles) at its maximum, and a biexponential fit (solid line).

N$_3$VH^0 through HPHT annealing of a nitrogen doped CVD diamond, evident from the growth in absorption strength of the 3107 cm^{-1} LVM after annealing, while the 3123 cm^{-1} mode of NVH^0 is removed.[9,10] Further details of these samples are provided in the Supporting Information.

Different peaks in the IR absorbance spectra of hydrogen-rich diamonds, such as evident in Figure 1c, have been speculatively attributed to different overtones and combinations of the stretch and bend modes of N$_3$VH^0 (see Table S1, Supporting Information).[16−20] These modes have weak (but nonzero) matrix elements as a result of the anharmonicity of the potential energy. However, unique assignments of the rich vibrational spectra are challenging—in particular it is difficult to isolate the overtones of C−H stretches when different defects are present. Further, steady-state absorbance spectra do not provide unique information about the dynamics of vibrational relaxation, such as the excited state lifetime, T_1. The line width Γ of an individual absorption peak provides some information about T_1, since

$$\Gamma = 1/2\pi T_1 + 1/\pi T_2^* + \Gamma_{\text{in}} \qquad (1)$$

but the line width also contains contributions from pure dephasing (T_2^*) and inhomogeneous broadening (Γ_{in}); hence, T_1 is difficult to extract from Fourier Transform Infrared (FTIR) spectroscopy.

To determine the excited state lifetime, T_1, we used transient vibrational absorption spectroscopy (TVAS), a pump−probe technique that detects the differences in vibrational absorption created following IR photoexcitation. The photoexcitation pulse was resonant to the 3107 cm^{-1} (ν_S) LVM, with a spectral bandwidth that was narrowed to avoid overlap with the nearby 3237 cm^{-1} LVM. The broad-band probe either was tuned resonantly to ν_S or set to probe other spectral ranges (ν_{probe} = 2800−3300 cm^{-1}). A full description of our experimental setup is detailed in the Supporting Information (Figure S1). An approach based on ultrafast spectroscopy in the visible range as reported by Ulbricht et al. is not applicable here, as there are no electronic states associated with N$_3$VH^0 in the diamond band gap.

The transient absorption spectra from sample N1 are presented in Figure 2a at different pump−probe time delays, Δt. We first draw attention to the degenerate pump−probe
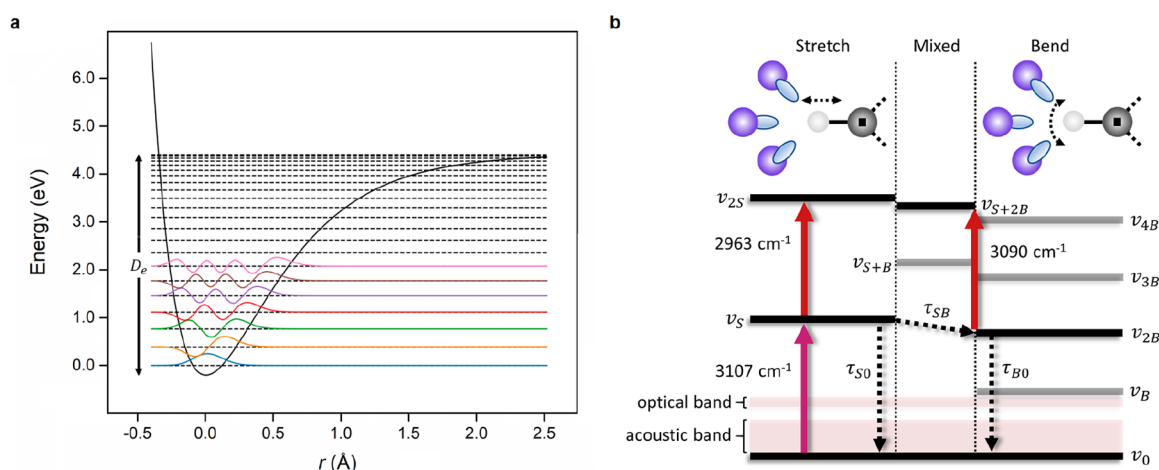
Figure 3. Anharmonic potential, vibrational structure, excitation, and decay pathways associated with the N_3VH^0 defect. (a) Morse potential energy well of the C−H stretch along bond length r. (b) Energy level diagram of the vibrational structure of N_3VH^0. After the C−H stretch is photoexcited from $n = 0$ to $n = 1$, extra absorption occurs at 2963 cm^{-1} from $n = 1$ to $n = 2$. Anharmonic coupling to the bend modes provides population in the v_{2B} state, evidenced by excited state absorption at 3090 cm^{-1}.

spectrum ($v_{pump} = v_{probe} = 3107$ cm^{-1}), Figure 2a right. A ground state bleach (GSB) is clearly evident: centered at 3107 cm^{-1}, its negative sign indicates a reduction in the ground state population, N_0. A nondegenerate probe (left) revealed a strong excited state absorption (ESA) feature at 2963 cm^{-1}, labeled ESA$_S$. After the 3107 cm^{-1} pump pulse excited the stretch mode from the ground state to v_S, electric dipole-allowed absorption of the probe can occur from v_S to v_{2S}.

The ESA$_S$ feature was observed at a smaller wavenumber than the GSB, as the potential energy function along the C−H stretch is anharmonic. The quantized vibrational states have energies E_n, where $n = 0, 1, 2...$, and have a progressively smaller separation in energies between adjacent levels. The direct observation of ESA$_S$ between vibrational states 1 and 2 further allows the weak 6070 cm^{-1} (= 3107 + 2963) cm^{-1} IR absorption peak (Figure 1b) to be uniquely assigned to the $n = 2 \leftarrow n = 0$ transition. The low absorption strength for this $\Delta n = 2$ transition is a direct consequence of its small matrix element, which is electric-dipole-forbidden for a harmonic potential. Density functional theory modeling using the AIMPRO program (see Supporting Information) determined the v_{2S} state to appear at 6106 cm^{-1}. This corroborates with assignment of the FTIR absorption feature at 6070 cm^{-1} to v_{2S}. Thus, $v_{2S} - v_S$ was inferred through FTIR spectroscopy to be 2963 cm^{-1} and validated by the prediction of 2999 cm^{-1} from theory.

To model analytically the potential energy function, $V(r)$, for the C−H stretch, we adopted the Morse potential (see Supporting Information for a full description), $V(r) = D_e(1 - e^{-a(r-r_e)})^2$. This approach follows the change in potential energy due to moving from the equilibrium position, r_e, of the C−H bond. It is parametrized by the energetic depth, D_e, and inverse width, a, of an anharmonic potential well, which is shown in Figure 3a. The energy spacings (3107 and 2963 cm^{-1}) directly obtained from TVAS allowed both $D_e = 4.56$ eV and $a = 1.99 \times 10^{10}$ m^{-1} to be determined. The Morse potential is particularly convenient, as it allows the matrix elements D_{ij}, and hence the optical absorption coefficient, to be calculated directly with the defect concentration as the only free parameter. Through this method, we predict dimensionless matrix elements of 0.104 for the excitation $v_S \leftarrow v_0$ and 0.149 for the transition $v_{2S} \leftarrow v_S$. These numbers corroborate the

experimental ratio of the amplitude of the ESA$_S$ feature ($\Delta \alpha_{12}$) to that of the GSB ($\Delta \alpha_{01}$): the Morse potential model predicts $\frac{\Delta \alpha_{12}}{\Delta \alpha_{01}} = -\frac{D_{12}^2}{2D_{01}^2} = -1.03$, whereas the transient absorption spectra yield $\frac{\Delta \alpha_{12}}{\Delta \alpha_{01}} = -1.13$.

By using the measured absorption and the matrix elements from the Morse potential model, we can determine the concentration of N_3VH^0, assuming optical absorption occurs between two quantum states with a Lorentzian line shape (Supporting Information, Sections S6 and S7). This condition is straightforwardly satisfied for sample S1, which exhibited a Lorentzian absorption spectrum around 3107 cm^{-1}, and for which we estimate a N_3VH^0 concentration of 4 ppm. This provides the following calibration factor that allows the integrated area of the 3107 cm^{-1} peak, I_{3107}, to be converted into a concentration of N_3VH^0: $[N_3VH^0]$(ppb) = (110 ± 10) × I_{3107}(cm^{-2}). For the natural diamonds, which exhibited inhomogeneous line broadening caused by strain induced by the high number of point defects (Supporting Information), we instead use the Lorentzian component of a Voigt fit and can similarly estimate $[N_3VH^0]$.

To verify the estimate of the N_3VH^0 concentration from our method, we used two approaches: (1) Using the known relationship between absorption strength and concentration for the NVH^0 defect (see Supporting Information S8), the predicted concentration of N_3VH^0 in sample S1 is 7.6 ± 0.8 ppm. This is similar in magnitude to the value of 4 ppm obtained using the Morse potential and the line width and seems reasonable given the assumptions used in both methods. (2) Estimating the upper limit of $[N_3VH^0]$ from the total nitrogen concentration (in all different forms) in the as-grown CVD diamond sample, and that which cannot be accounted for in defects other than N_3VH^0 after HPHT annealing. In this way, we estimate that the maximum concentration of N_3VH^0 is less than ~10 ppm in S1, which is consistent with the other results.

Turning now to the vibrational dynamics, Figure 2b reports the modulus of the absorption change for the GSB and ESA$_S$ features versus pump−probe delay, as seen in natural diamond N1. The GSB transient shows a multicomponent decay—an initial rapid decay followed by a second slower decay—with

associated time constants τ_1 and τ_2. We attribute τ_1 to a fast energy transfer via the LVMs of the nitrogen atoms, or into the diamond lattice itself.[23] A fuller treatment of these data, to extract time constants for individual processes, is detailed later on in the paper. To estimate the average population decay rate, we took a weighted average of the two components from the biexponential fit to ESA_S, obtaining Γ_{TVAS} for the 3107 cm^{-1} feature in each sample. This enables a comparison with the Lorentzian component of the line width, $\Gamma_{FTIR, Lorentz}$, for the LVM, which by eq 1 may have components from population relaxation (T_1) and pure dephasing (T_2^*). For N1, $\Gamma_{FTIR, Lorentz}$ = 2.4 cm^{-1} and Γ_{TVAS} = 2.5 cm^{-1}, and similar agreement was found for N2 and S1 (see Table S2). Therefore, the population relaxation rate accounts for the homogeneous line width in equilibrium, and pure dephasing does not contribute substantially, as reported for hydrogen defects in silicon.[24−26] Further, in Figure 2a, the line width of ESA_S can be seen to be broader than the line width of the GSB. This can be understood as the ESA_S line width additionally containing the population relaxation rate of n = 2 (see Figure S5).

Notably, the dynamics evident in Figure 2b show that the decay lifetime of the ESA_S feature (τ_2 = 3.3 ± 0.2 ps), indicative of the rate at which n = 1 is depopulated, is markedly shorter than the lifetime of the GSB (τ_2 = 6.2 ± 0.2 ps), which tracks the recovery of the ground-state absorption. This suggests that rather than a single decay channel from n = 1, a more complex decay pathway is required to understand the vibrational dynamics, involving at least one additional state coupled to n = 1. The presence of a weak excited state absorption feature at 3090 cm^{-1}, labeled ESA_B in Figure 2a, gives further evidence of an intermediate state that is critically involved in the relaxation pathway of the C−H stretch. Figure 2c shows that absorbance at ESA_B is delayed (cf. ESA_S which decays from Δt = 0), indicating an excited state that is populated from the initially populated v_S. We recorded similar spectra for the other samples (see Figure S2). Despite the vast difference among N1, N2, and S1, in terms of sample origin, and concentrations of N_3VH^0 and nitrogen in total, we obtained similar population relaxation times for all three diamonds (see Supporting Information, Tables S2 through S5).

Based on the above, we propose the following mechanism for the vibrational excitation and decay of the 3107 cm^{-1} C−H stretch, schematically illustrated in Figure 3b. The pump pulse, centered at 3107 cm^{-1}, photoexcites the v_S state. This leads to the appearance of the GSB feature at 3107 cm^{-1}, as shown in Figure 2a. The population now in v_S creates additional absorption into v_{2S} for the probe pulse (at 2963 cm^{-1}), producing ESA_S. Decay from v_S occurs either (1) directly (to v_0) or (2) indirectly via the first overtone of the bend mode, v_{2B}. These two processes proceed synchronously but occur at different rates, creating a difference between the decay times of GSB and ESA_S features. The direct pathway (i.e., $v_S \rightarrow v_0$) likely proceeds through a nonradiative multiphonon relaxation involving emission of two optical phonons and one acoustic phonon, cf. analogous experiments carried out on hydrogen-related modes in the silicon lattice.[24−26]

We suggest that ESA_B at 3090 cm^{-1} corresponds to excitation from v_{2B} to the combination band v_{S+2B}, the doubly excited bend mode having been populated from decay of the initially populated stretch mode, v_S, as pictured in Figure 3b (i.e., the indirect pathway). Confidence in this assignment is based on the following: (1) the IR absorbance features (see

Table S1) which predicts that $v_{S+2B} - v_{2B}$ = 3101 cm^{-1}, within error of the wavenumber of ESA_B; (2) Symmetry analysis (see Table S1) which reveals that the transition from v_S to v_{2B} is allowed by symmetry, unlike the symmetry-forbidden transition from v_S to v_B; and (3) Energy conservation: emission of a single acoustic phonon can provide the energy change required to transfer to the v_{2B} state, whereas at least two phonons would be required to access v_B. One-phonon emission is expected to occur faster than higher order reactions requiring two or more phonons. We cannot however rule out the possibility that ESA_B is due to excitation from v_B to v_{S+B}, which would be a better numerical match to its wavenumber (from the IR, $v_{S+B} - v_B$ = 3091 cm^{-1}) but goes against both the symmetry and energy arguments.

The temperature-dependent decay dynamics (see Table S3 and Figure S3) provide further information: the lifetime of the GSB exhibits a significant increase to 12.2 ps, almost doubling upon cooling to 100 K, but no analogous change is observed in the lifetime of ESA_S. To account for the different temperature dependences of the GSB and ESA_S, we suggest that only the indirect pathway (via the bend modes) is temperature dependent. For instance, if that pathway is mediated by acoustic phonons, whose population is reduced at lower temperatures, a slower GSB decay would result, as observed. A number of multiphonon processes are possible for nonradiative decay from v_{2B}, some including relaxation via v_B.

A kinetic model comprised of rate equations (see Supporting Information) based on the processes shown in Figure 3b replicates the observed data, including the dynamics of the GSB, ESA_S, and ESA_B together. The fit to data from N1, shown in Figure S6, gives estimate time constants for each of the three processes: τ_{S0} = 6.9 ± 0.2 ps, τ_{SB} = 6.4 ± 0.2 ps, and τ_{B0} = 5.6 ± 0.4 ps. The similarity in these values allows for competition between the direct and indirect decays, leading to the disparity in lifetime between ESA_S and the GSB. Through our fitting, we estimated the dimensionless matrix element for excitation from $v_{2B} \rightarrow v_{S+2B}$ to be 0.157. This number fits reasonably well with our derived values from the Morse potential calculations, which gives credence to our assignment of ESA_B to a transition associated with the C−H stretch.

Our results demonstrate a significantly longer lifetime ($\tau_{S0} \approx$ 7 ps) for the vibrational relaxation of the LVM of N_3VH^0 in comparison to the faster lifetime reported for NV^- by Ulbricht et al.[27] We attribute this difference to the larger energy spacing between the vibrational levels in N_3VH^0, which is more than twice the optical phonon energy (Figure 3b). Thus, energy relaxation via the diamond lattice is slow for this LVM of N_3VH^0. In contrast, for NV^- the energy spacing is comparable to the optical phonon energy, and vibrational energy relaxation is fast.

In summary, we have successfully shown that ultrafast spectroscopy can be employed in the infrared region to determine the lifetimes for decay or recovery of vibrational modes in the N_3VH^0 defect in diamond. Our results confer information about the mechanism for the decay of the excited stretch (v_S) mode. The observation of an excited state absorption at 2963 cm^{-1} confirms that the v_{2S} state lies at 6070 cm^{-1} in the IR absorption and quantifies the anharmonicity of the stretch mode. Calculations based on the Morse potential allowed us to deduce the concentration of N_3VH^0, in reasonable agreement with values derived from other methods. From this, we were able to estimate the oscillator strength for the C−H stretch mode in N_3VH^0,

thereby relating FTIR peak intensity to defect concentration directly for this prominent defect, which is the most stable form of both nitrogen and hydrogen in diamond. With regards to the vibrational dynamics, decay from ν_S occurs through two separate pathways—a direct decay back down to the ground state, and an indirect relaxation via the excited two-bend (ν_{2B}) mode of the C−H bond. These decays occur at different rates, producing an overall lifetime for the recovery of the ground state that is an amalgamation of the two. The experimental and theoretical methodology developed in this study is broadly applicable to the infrared-active vibrational modes of other atomic-scale defects, both in diamond and in other materials. Hence, it is now possible to determine decay pathways, establish the energetic landscape of local vibrational modes, and quantify defect concentrations, for a wide suite of defects of interest in optical and electronic applications.

■ ASSOCIATED CONTENT

Ⓢ Supporting Information

The Supporting Information is available free of charge at https://pubs.acs.org/doi/10.1021/acs.jpclett.0c01806.

> Symmetry character of N_3VH^0's local vibrational modes; Sample details; Infrared absorption spectra; TVAS experimental method; First-principles calculation of the C−H stretch in N_3VH^0; Model via the Morse potential; N_3VH^0 concentration from the absorption coefficient; Calibration factor for the 3123 cm^{-1} feature in NVH^0; Estimate of FTIR line width from TVAS lifetime; Additional TVAS experimental data; Kinetic model of a three-level system. (PDF)

■ AUTHOR INFORMATION

Corresponding Authors

James Lloyd-Hughes − *Department of Physics, University of Warwick, Coventry CV4 7AL, United Kingdom;* ⓞ orcid.org/0000-0002-9680-0138; Email: j.lloyd-hughes@warwick.ac.uk

Vasilios G. Stavros − *Department of Chemistry, University of Warwick, Coventry CV4 7AL, United Kingdom;* ⓞ orcid.org/0000-0002-6828-958X; Email: v.stavros@warwick.ac.uk

Mark E. Newton − *Department of Physics, University of Warwick, Coventry CV4 7AL, United Kingdom;* Email: m.e.newton@warwick.ac.uk

Authors

Daniel J. L. Coxon − *Department of Physics and Department of Chemistry, University of Warwick, Coventry CV4 7AL, United Kingdom; EPSRC Centre for Doctoral Training in Diamond Science and Technology, Warwick, United Kingdom*

Michael Staniforth − *Department of Physics and Department of Chemistry, University of Warwick, Coventry CV4 7AL, United Kingdom*

Ben G. Breeze − *Department of Physics and Department of Chemistry, University of Warwick, Coventry CV4 7AL, United Kingdom*

Simon E. Greenough − *Department of Chemistry, University of Warwick, Coventry CV4 7AL, United Kingdom*

Jonathan P. Goss − *School of Engineering, Newcastle University, Newcastle upon Tyne NE1 7RU, United Kingdom*

Maurizio Monti − *Department of Physics, University of Warwick, Coventry CV4 7AL, United Kingdom;* ⓞ orcid.org/0000-0003-2192-3747

Complete contact information is available at:
https://pubs.acs.org/10.1021/acs.jpclett.0c01806

Notes

The authors declare no competing financial interest.

■ ACKNOWLEDGMENTS

■ REFERENCES

(1) Doherty, M. W.; Manson, N. B.; Delaney, P.; Jelezko, F.; Wrachtrup, J.; Hollenberg, L. C. L. The nitrogen-vacancy colour center in diamond. *Phys. Rep.* **2013**, *528*, 1−45.

(2) Jelezko, F.; Wrachtrup, J. Single defect centers in diamond: A review. *Phys. Status Solidi A* **2006**, *203*, 3207−3225.

(3) Awschalom, D. D.; Hanson, R.; Wrachtrup, J.; Zhou, B. B. Quantum technologies with optically interfaced solid-state spins. *Nat. Photonics* **2018**, *12*, 516−527.

(4) Ashfold, M. N. R.; Goss, J. P.; Green, B. L.; May, P. W.; Newton, M. E.; Peaker, C. V. Nitrogen in Diamond. *Chem. Rev.* **2020**, *120*, 5745−5794.

(5) Isberg, J.; Hammersberg, J.; Johansson, E.; Wikström, T.; Twitchen, D. J.; Whitehead, A. J.; Coe, S. E.; Scarsbrook, G. A. High carrier mobility in single-crystal plasma-deposited diamond. *Science* **2002**, *297*, 1670−1672.

(6) Glover, C.; Newton, M. E.; Martineau, P. M.; Quinn, S.; Twitchen, D. J. Hydrogen incorporation in diamond: The vacancy-hydrogen complex. *Phys. Rev. Lett.* **2004**, *92*, 135502.

(7) Glover, C.; Newton, M. E.; Martineau, P.; Twitchen, D. J.; Baker, J. M. Hydrogen incorporation in diamond: The nitrogen-vacancy-hydrogen complex. *Phys. Rev. Lett.* **2003**, *90*, 185507.

(8) Maier, F.; Riedel, M.; Mantel, B.; Ristein, J.; Ley, L. Origin of surface conductivity in diamond. *Phys. Rev. Lett.* **2000**, *85*, 3472−3475.

(9) Khan, R. U. A.; Cann, B. L.; Martineau, P. M.; Samartseva, J.; Freeth, J. J. P.; Sibley, S. J.; Hartland, C. B.; Newton, M. E.; Dhillon, H. K.; Twitchen, D. J. Colour-causing defects and their related optoelectronic transitions in single crystal CVD diamond. *J. Phys.: Condens. Matter* **2013**, *25*, 275801.

(10) Khan, R. U. A.; Martineau, P. M.; Cann, B. L.; Newton, M. E.; Twitchen, D. J. Charge transfer effects, thermo and photochromism in single crystal CVD synthetic diamond. *J. Phys.: Condens. Matter* **2009**, *21*, 364214.

(11) Stachel, T.; Luth, R. W. Diamond formation - Where, when and how? *Lithos* **2015**, *220*, 200−220.

(12) Kiflawi, I.; Fisher, D.; Kanda, H.; Sittas, G. The creation of the 3107 cm^{-1} hydrogen absorption peak in synthetic diamond single crystals. *Diamond Relat. Mater.* **1996**, *5*, 1516−1518.

(13) Charles, S. J.; Butler, J. E.; Feygelson, B. N.; Newton, M. E.; Carroll, D. L.; Steeds, J. W.; Darwish, H.; Yan, C. S.; Mao, H. K.; Hemley, R. J. Characterization of nitrogen doped chemical vapor

deposited single crystal diamond before and after high pressure, high temperature annealing. *Phys. Status Solidi A* **2004**, *201*, 2473−2485.

(14) Charette, J. J. Le spectre infra-rouge a grande dispersion des trois types de diamants et ses variations en fonction de la temperature. *Physica* **1959**, *25*, 1303−1312.

(15) Woods, G. S.; Collins, A. T. Infrared absorption spectra of hydrogen complexes in type I diamonds. *J. Phys. Chem. Solids* **1983**, *44*, 471−475.

(16) Davies, G.; Collins, A. T.; Spear, P. Sharp infra-red absorption lines in diamond. *Solid State Commun.* **1984**, *49*, 433−436.

(17) De Weerdt, F.; Kupriyanov, I. N. Report on the influence of HPHT annealing on the 3107 cm^{-1} hydrogen related absorption peak in natural type Ia diamonds. *Diamond Relat. Mater.* **2002**, *11*, 714−715.

(18) De Weerdt, F.; Pal'yanov, Y. N.; Collins, A. T. Absorption spectra of hydrogen in ^{13}C diamond produced by high-pressure, high-temperature synthesis. *J. Phys.: Condens. Matter* **2003**, *15*, 3163−3170.

(19) Rondeau, B.; Fritsch, E.; Guiraud, M.; Chalain, J. P.; Notari, F. Three historical 'asteriated' hydrogen-rich diamonds: Growth history and sector-dependent impurity incorporation. *Diamond Relat. Mater.* **2004**, *13*, 1658−1673.

(20) Fritsch, E.; Hainschwang, T.; Massi, L.; Rondeau, B. Hydrogen-Related Optical Centers in Natural Diamond: An Update. *New Diam. Front. Carbon Technol.* **2007**, *17*, 63−89.

(21) Kohn, S. C.; Speich, L.; Smith, C. B.; Bulanova, G. P. FTIR thermochronometry of natural diamonds: A closer look. *Lithos* **2016**, *265*, 148−158.

(22) Goss, J. P.; Briddon, P. R.; Hill, V.; Jones, R.; Rayson, M. J. Identification of the structure of the 3107 cm^{-1} H-related defect in diamond. *J. Phys.: Condens. Matter* **2014**, *26*, 145801.

(23) Gentile, F. S.; Salustro, S.; Causa, M.; Erba, A.; Carbonniere, P.; Dovesi, R. The VN$_3$H defect in diamond: A quantum-mechanical characterization. *Phys. Chem. Chem. Phys.* **2017**, *19*, 22221−22229.

(24) Budde, M.; Lüpke, G.; Parks Cheney, C.; Tolk, N. H.; Feldman, L. C. Vibrational Lifetime of Bond-Center Hydrogen in Crystalline Silicon. *Phys. Rev. Lett.* **2000**, *85*, 1452−1455.

(25) Budde, M.; Lüpke, G.; Chen, E.; Zhang, X.; Tolk, N. H.; Feldman, L. C.; Tarhan, E.; Ramdas, A. K.; Stavola, M. Lifetimes of Hydrogen and Deuterium Related Vibrational Modes in Silicon. *Phys. Rev. Lett.* **2001**, *87*, 145501.

(26) Lüpke, G.; Tolk, N. H.; Feldman, L. C. Vibrational lifetimes of hydrogen in silicon. *J. Appl. Phys.* **2003**, *93*, 2317−2336.

(27) Ulbricht, R.; Dong, S.; Gali, A.; Meng, S.; Loh, Z. H. Vibrational relaxation dynamics of the nitrogen-vacancy center in diamond. *Phys. Rev. B: Condens. Matter Mater. Phys.* **2018**, *97*, 220302.

Supporting Information for: An Ultrafast Shakedown Reveals the Energy Landscape, Relaxation Dynamics and Concentration of the N_3VH^0 Defect in Diamond

Daniel J. L. Coxon,[†,‡,¶] Michael Staniforth,[†,‡] Ben G. Breeze,[†,‡] Simon E. Greenough,[‡] Jonathan P. Goss,[§] Maurizio Monti,[†] James Lloyd-Hughes,[,†] Vasilios G. Stavros,[*,‡] Mark E. Newton,[*,†]*

† Department of Physics and ‡ Department of Chemistry, University of Warwick, Gibbet Hill Road, Coventry CV4 7AL, United Kingdom

¶ EPSRC Centre for Doctoral Training in Diamond Science and Technology, United Kingdom

§ School of Engineering, Newcastle University, Newcastle upon Tyne NE1 7RU, United Kingdom

CORRESPONDING AUTHORS

*j.lloyd-hughes@warwick.ac.uk *v.stavros@warwick.ac.uk *m.e.newton@warwick.ac.uk

S1. Symmetry character of N_3VH^0's local vibrational modes

We determined the symmetry character of each level according to the following rules: (1) The

n^{th} overtone of a nondegenerate vibration has symmetry character equal to the nth exponent of

the fundamental. (2) Combination band symmetry is the direct product of the symmetry of

individual levels. (3) The nth overtone of a degenerate vibration has symmetry character $\chi_E^n(R)$:

$$\chi_E^n(R) = \tfrac{1}{2}[\chi_E^{n-1}(R)\chi_E(R) + \chi_E(R^n)],$$

where $\chi_E(R^n)$ is the symmetry character of the operation R performed n consecutive times.[SR1]

The results are listed in Table S1. Phonon processes are allowed only if the two levels involved

in the process have equivalent symmetry. The assignment to particular N_3VH^0 stretch and bend

modes, and their combinations and overtones, is based on our IR absorption and transient

absorption spectra.

Table S1. Vibrational features relating to N_3VH^0 observed in N1. The wavenumber of our

observed IR absorption peaks (ω_{obs}) is compared to the literature (ω_{ref}). The references

correspond to those listed in the manuscript.

N₃V:H mode	ω_{obs} (cm^{-1})	ω_{ref} (cm^{-1})	Reference	Symmetry Character
ν_B	1405	1405	(14)	E
ν_{2B}	2787	2786	(16)	$A_1 + E$
ν_S	3107	3107	(14)	A_1
ν_{3B}	4169	4169	(16)	$A_1 + A_2 + E$
ν_{S+B}	4496	4499	(16)	E
ν_{4B}	N/A	5555	(20)	$A_1 + 2E$
ν_{S+2B}	5888	5889	(16)	$A_1 + E$
ν_{2S}	6070	6070	(20)	A_1

S2. Sample details

Natural sample N1 originated from the Argyle mine (Western Australia), where diamonds are typically rich in N_3VH^0.[SR2] Natural sample N2 was supplied by De Beers Group Technology. It was subject to annealing at 2000 °C to grow in N_3VH^0. Synthetic sample S1, provided by Dr Danielle A. Braje MIT Lincoln Laboratory, was grown by CVD and HPHT annealed at 2200 °C. In the setup, a sample is mounted over a small hole in a metal plate, which slides into a mount attached to X, Y and Z stages. We align the sample so that it is oriented with the overlapping pump and probe beams perpendicular to the (100) face, facilitating absorption from both the stretch and bend modes.

S3. Infrared absorption spectra

A Perkin Elmer Spectrum GX FTIR spectrometer, with a spectral resolution of 0.25 cm^{-1}, was used to obtain FTIR spectra at room temperature. These were calibrated by setting the absorption coefficient of diamond at 2000 cm^{-1} to its literature value (12.3 cm^{-1}). A Bruker IFS66 FTIR spectrometer, with a spectral resolution of 0.25 cm^{-1}, was used to record FTIR spectra at 100K and 10K. Samples were mounted inside an Oxford Instruments MicroStatHe. Temperature control was achieved through an Oxford Instruments ITC503. Absorption of the crystalline quartz windows limited the spectral window to the 3000–3500 cm^{-1} range for our temperature-dependent experiments.

S4. TVAS experimental method

The TVAS experimental setup has not been described elsewhere; as such, we provide extra details herein, in addition to the specifics relating to our measurements. We use a MKS Newport-SpectraPhysics MaiTai SP Ti:sapphire laser to produce an 800 nm pulse train (84 MHz repetition rate, average power >400 mW) with horizontal polarisation. One pulse is subsequently amplified by two regenerative amplification stages within a Spitfire ACE. Each amplification stage is pumped by an Ascend laser (527 nm light, 1 kHz repetition rate, average

power >35 W). This produces 800 nm laser pulses, at a repetition rate of 1 kHz and a pulse duration of <40 fs, and an average power of >13 W. Two portions of this beam are used to pump two tuneable optical parametric amplification systems (TOPASs), which create IR pulses with peak wavenumber tuneable in the range 700-10000 cm^{-1}, and a bandwidth of roughly 500 cm^{-1}. The pump pulse (ω = 3107 cm^{-1}, P = 1.56 mW, 370 μm spot size, fluence = 1.44 mJ cm^{-2}) first enters a pulse shaper to be spectrally narrowed. The pulse shaper setup spreads out the IR pump pulse using a diffraction grating (3.5 μm blaze, 300 lines mm^{-1} resolution). Light is then collimated through an adjustable slit onto a flat mirror. This reflects light back down the optical line into the lens, which refocuses light back onto the grating, to be re-collimated. The overall effect of the pulse shaper is to spectrally narrow the IR pump to a reduced bandwidth of 250 cm^{-1}. Crucially, this ensures that the pulse is sufficiently short in time (<100 fs) to capture the dynamics whilst only photoexciting the 3107 cm^{-1} mode. Therefore, we can attribute all our observations to the excitation of only the N_3VH^0 stretch mode. Before reaching the sample, the pump pulse passes through an optical chopper, rotating at 500 Hz to block every other pulse. This allows a direct comparison between signal detection of pumped and unpumped sample. A TVAS spectrum represents a difference in optical density (ΔOD) between pump-off, $I_{pr}(\lambda, \infty)$, and pump-on signal, $I_{pr}(\lambda, \Delta t)$, at time Δt.[SR3] The probe pulse (ω = 3107 cm^{-1}, P = 0.78 mW, 360 μm spot size, fluence = 0.77 mJ cm^{-2}) is polarized at 90° to the pump to minimize interference between the two beams. A gold retro-reflector in the probe line is mounted on a moveable stage. We use this to vary the time delay, Δt, between the two pulses over a 3.3 ns window, with a time resolution of 17 fs. It is partitioned equally by a CaF$_2$ beamsplitter to a reference pulse and a probe pulse. The reference pulse does not pass through the sample. It is detected to subtract shot-to-shot laser noise. For detection, probe light enters a HORIBA iHR320 imaging spectrometer, where it is dispersed by a diffraction grating (4 μm blaze, 300 lines mm^{-1} resolution) onto a Mercury Cadmium Telluride (MCT) detector array.

This detector (contained within an Infrared Systems Development FPAS-0144) is comprised of two 64-pixel linear arrays – one each for the probe and reference pulses. It is cooled using liquid nitrogen to eliminate thermal contributions to the signal. We used a Perkin Elmer mid-IR polystyrene reference card to calibrate pixel number to wavenumber. The change in optical density is:

$$\Delta OD = \log_{10}\left(\frac{I_{pr}(\lambda,\infty)}{I_{pr}(\lambda,\Delta t)}\frac{I_{ref}(\lambda,\Delta t)}{I_{ref}(\lambda,\infty)}\right),$$

where $I_{ref}(\lambda,\infty)$ denotes the reference signal measured during pump-off and $I_{ref}(\lambda,\Delta t)$ is the reference signal measured during pump-on, at time Δt. Figure S1 shows a representation of our TVAS experimental setup.
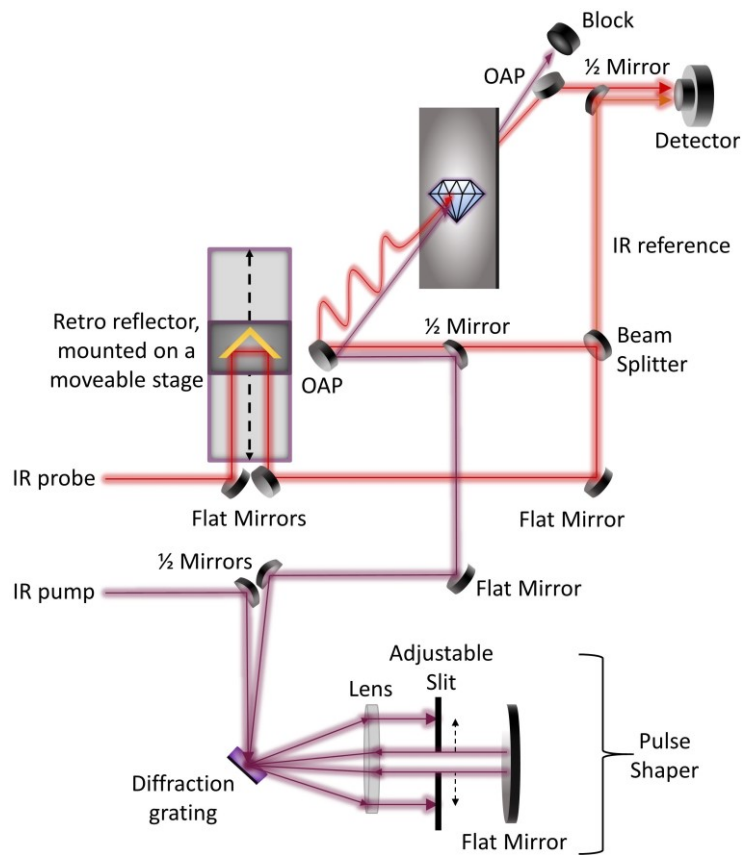

Figure S1. Schematic representation of our TVAS experimental setup. Note: OAP stands for off-axis parabolic mirror.

S5.   First-principles calculation of the C–H stretch in N_3VH^0

To create an optimized theoretical model of the N_3VH^0 defect, the AIMPRO code was used to carry out local density approximation (LDA) density functional theory (DFT) calculations on 216 atom supercells. The potential shape is generated by calculating the total energy as a function of the displacement of a hydrogen atom along the [111] axis. A more complete description of the model and its parameters is detailed in Ref. 19. The oscillator mass, a reduced mass used to solve the 1D Schrödinger equation, is dependent on contributions from the hydrogen atom and from the carbon lattice. It was set such as to fix the fundamental vibrational wavenumber to 3107 cm^{-1}.

S6.   Model via the Morse potential

We approximated the potential energy, $V(r)$, of the stretch mode along the C–H bond direction using the Morse potential:

$$V(r) = D_e(1 - e^{-a(r-r_e)})^2,$$

where D_e is the depth of the potential well, a is the inverse width of the well and r_e is the equilibrium position. The solution to the Schrödinger equation for the vibrational states $n = 0, 1, 2 \dots$ gives the quantized energy levels, E_n, via:

$$E_n = E_0(n + 1/2) - \frac{E_0^2(n+1/2)^2}{4D_e},$$

where E_0 is the zero-point energy. The depth and inverse width of the potential well can be calculated from the experimentally determined spacing between energy levels using:

$$D_e = \frac{(2E_{10}-E_{21})^2}{2(E_{10}-E_{21})} \text{ and}$$

$$a = \frac{E_0}{\hbar}\sqrt{\frac{\mu}{2D_e}},$$

where μ is the reduced mass of the stretch mode and E_{ij} is the energy difference between the ith and j^{th} energy levels.

   The solution of the Schrödinger equation determines the wavefunctions, ψ_n, of the vibrational states, which can be written for convenience in dimensionless coordinates $z =$

$2\lambda e^{-(x-x_e)}$, where $x = ar$, $x_e = ar_e$ and $\lambda = \sqrt{2\mu D_e}/(a\hbar)$. For the vibrational states $n = 0, 1, 2 \dots [\lambda - 1/2]$ the wavefunctions are:

$$\psi_n(z) = N_n z^{\alpha/2} e^{-z/2} L_n^{(\alpha)}(z),$$

where $\alpha = 2\lambda - 2n - 1$, $L_n^{(\alpha)}(z)$ are the generalized Laguerre polynomials, and

$$N_n = \left(\frac{n!\alpha}{\Gamma(2\lambda-n)}\right)^{1/2}.$$

Then the wavefunctions in terms of r, normalized such that $\int_0^\infty \psi_n^*(r)\psi_n(r)dr = 1$, can be determined from:

$$\psi_n(r) = \sqrt{a}\psi_n(z).$$

The transition rate from the ith to the jth energy level was determined from Fermi's golden rule in the electric dipole approximation. It is proportional to D_{ij}^2, where:

$$D_{ij} = e\langle\psi_j|x|\psi_i\rangle/a,$$

and the matrix element was determined analytically from

$$\langle\psi_j|x|\psi_i\rangle = \frac{2(-1)^{j-i+1}}{(j-i)(2N-i-j)}\sqrt{\frac{(N-i)(N-j)\Gamma(2N-j+1)j!}{\Gamma(2N-i+1)i!}}.$$

The determined dimensionless matrix elements were as follows: $\langle\psi_1|x|\psi_0\rangle = 0.150$, $\langle\psi_2|x|\psi_0\rangle = -0.016$ and $\langle\psi_2|x|\psi_1\rangle = 0.215$. As the probe light shines onto the (100) surface of the diamond, it is not parallel to the [111] direction of the C–H bond in N_3VH^0. To account for this, we reduce each dimensionless matrix element by a factor of $\sqrt{3}$.

S7. N_3VH^0 concentration from the absorption coefficient

At low defect concentrations, where inhomogeneous broadening can be ignored, the following relationship exists between the full width at half maximum (Γ) and the total dephasing lifetime (T_2) – which includes the excited state lifetime (T_1) and the pure dephasing time (T_2^*):

$$\Gamma = \frac{1}{\pi T_2} = \frac{1}{2\pi T_1} + \frac{1}{\pi T_2^*}.$$

For a two-level system, the absorption coefficient $a_{01}(\omega)$ for an optical transition from the ground state ($n = 0$) to the 1ˢᵗ excited state ($n = 1$), is:[SR5]

$$\tag{1}$$

$$a_{01}(\omega) = \frac{D_{01}^2 \omega}{n_{op} \hbar c \varepsilon_0} \frac{1/T_2}{(\omega - \omega_{01})^2 + (1/T_2)^2} (N_0 - N_1),$$

where D_{01} is the dipole matrix element for the 0th to 1st energy level transition, ω is the frequency of light, $(N_0 - N_1)$ is the population difference between the $n = 0$ and $n = 1$ energy levels, n_{op} is the refractive index of the optical medium, c is the speed of light, ε_0 is the vacuum permittivity and ω_{01} is the angular frequency associated with the transition from $n = 0$ to $n = 1$. In equilibrium the ground state concentration is the defect concentration, as $N_0 = N_d$ and $N_1 = 0$ (thermal excitation of the 1st energy level is negligible). Hence Equation (1) can be fitted to the experimental absorption coefficient, which (assuming D_{01} from the Morse model) yields N_d along with T_2 and ω_{01}.

For the transient absorption case, the populations (N_0, N_1, N_2) for the three lowest states change from $(N_d, 0, 0)$ before photoexcitation has occurred to $(N_d - \delta N, \delta N, 0)$ immediately after photoexcitation. Hence Equation (1) predicts an absorption change $\Delta\alpha_{01} = \alpha_{01}^{pump\ on} - \alpha_{01}^{pump\ off} \propto -2\ \delta N\ D_{01}^2$ for the GSB and $\Delta\alpha_{12} \propto \delta N\ D_{12}^2$ for the ESA.

S8. Calibration factor for the 3123 cm^{-1} feature in NVH^0

The nitrogen-vacancy-hydrogen complex (NVH) is grown into nitrogen doped CVD diamond.[SR4] NVH^0 has an infrared absorption band at 3123 cm^{-1} for which oscillator strength has been calibrated by simultaneously measuring the change in concentration of NVH$^-$ by Electron Paramagnetic Resonance and that of the 3123 cm^{-1} band intensity when the relative concentrations of the two charge states are altered by heating or optical excitation.[SR6] The integrated area (in cm^{-2}) of the 3123 cm^{-1} absorption peak, I_{3123}, is related to the concentration of NVH^0 by the relation $[\text{NVH}^0](\text{ppb}) = (200 \pm 20) \times I_{3123}(\text{cm}^{-2})$. Using this same relation for N$_3$VH^0 would yield concentrations of 40.1 ppm for N1, 10.0 ppm for N2 and 7.6 ppm for S1.

S9. Estimate of FTIR linewidth from TVAS lifetime

We first determined a weighted-average estimate of the excited state lifetime, T_{av}, of the two lifetimes obtained from a bi-exponential fit of ESAs, according to the following equation:

$$T_{av} = \frac{A_1\tau_1 + A_2\tau_2}{(A_1+A_2)},$$

where A_X represents the amplitude, and τ_X the lifetime, of the exponential fit X. We subsequently used this value to derive an estimate of the linewidth, which in the case of negligible dephasing T_2^* and no inhomogeneous broadening is given by:

$$\Gamma_{TVAS} = \frac{1}{2\pi T_{av}}. \qquad (2)$$

Linewidths obtained from the TVAS experiments are shown in Table S2, alongside the total linewidth determined from a Voigt fit of the absorption feature at 3107 cm^{-1}, and the Lorentzian component thereof. The 3107 cm^{-1} LVM in the natural samples N1 and N2 are inhomogeneously broadened, while in the synthetic sample S1 the lineshape was purely Lorentzian, and hence was homogeneously broadened. Inhomogeneous broadening in the natural samples largely results from the close proximity of additional defects that can alter the C–H bond strength by the strain fields that they create. The total nitrogen concentration in the natural diamonds was well over 1000 ppm, of which N_3VH^0 contributed <22ppm (Table S2), whereas in S1 N_3VH^0 was the dominant impurity present.

Table S2. Linewidths determined from FTIR spectroscopy and from the transient absorption dynamics [Equation (2)], along with the concentration of N_3VH^0 estimated from the Morse potential method.

Sample	$\Gamma_{FTIR,total}$ (cm^{-1})	$\Gamma_{FTIR,Lorentz}$ (cm^{-1})	Γ_{TVAS} (cm^{-1})	$[N_3VH^0]$(ppm)
N1	4.0	2.4	2.5	21.8
N2	4.9	2.7	3.0	3.9
S1	2.1	2.1	2.5	4.2

S10. Additional TVAS experimental data

Table S3 details the time-constants and absolute amplitudes derived from the transient fits of

N1 that are shown in the main body text, alongside those from data taken at 100K. We obtained

similar room temperature transient fits of TVAS data for samples S1 and N2, as reported in

Figure S2. Tables S4 and S5 detail the time-constants obtained from these fits.

Table S3. Decay lifetimes from transient fits of data from the natural sample N1. Unless otherwise stated, measurements were taken at 298 K.

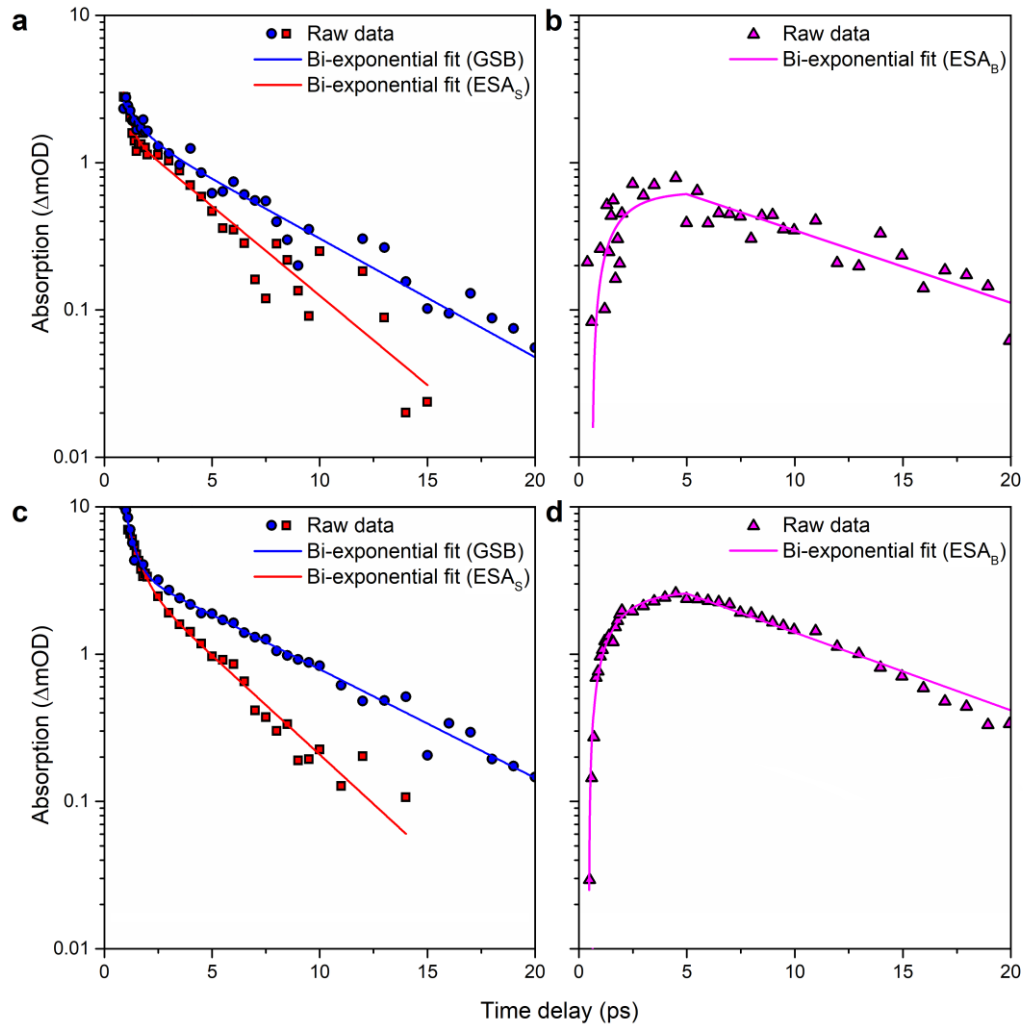|	$\omega(\text{cm}^{-1})$	A_1	$\tau_1(\text{ps})$	A_2	$\tau_2(\text{ps})$
GSB	3107	1.6 ($\pm$ 0.2)	0.44 ($\pm$ 0.09)	4.7 ($\pm$ 0.1)	6.2 ($\pm$ 0.2)
ESA$_S$	2963	2.6 ($\pm$ 0.2)	0.33 ($\pm$ 0.06)	4.1 ($\pm$ 0.2)	3.3 ($\pm$ 0.2)
ESA$_B$	3090	1.4 ($\pm$ 0.1)	1.5 ($\pm$ 0.3)	0.8 ($\pm$ 0.1)	8.4 ($\pm$ 1.6)
GSB, 100K	3107	1.0 ($\pm$ 0.1)	0.76 ($\pm$ 0.18)	1.1 ($\pm$ 0.1)	12.2 ($\pm$ 2.2)
ESA$_S$, 100K	2963	2.1 ($\pm$ 0.3)	0.49 ($\pm$ 0.11)	2.5 ($\pm$ 0.3)	4.1 ($\pm$ 0.5)

Figure S2. Absolute value transient fits of data from samples S1 and N2. **a,** GSB and ESA$_S$ (S1). **b,** ESA$_B$ (S1). **c,** GSB and ESA$_S$ (N2). **d,** ESA$_B$ (N2). These results are comparable to those reported for N1. Thus all samples have comparable energy relaxation dynamics.

Table S4. Decay lifetimes from transient fits of data from the synthetic sample S1. All measurements were taken at 298 K.

	$\omega(\text{cm}^{-1})$	A_1	$\tau_1(\text{ps})$	A_2	$\tau_2(\text{ps})$
GSB	3107	0.7 ($\pm$ 0.2)	0.69 ($\pm$ 0.25)	1.6 ($\pm$ 0.2)	5.4 ($\pm$ 0.7)
ESA$_S$	2963	1.2 ($\pm$ 0.2)	0.29 ($\pm$ 0.08)	1.8 ($\pm$ 0.2)	3.3 ($\pm$ 0.4)
ESA$_B$	3090	1.0 ($\pm$ 0.2)	1.3 ($\pm$ 0.5)	0.6 ($\pm$ 0.1)	8.9 ($\pm$ 2.2)

Table S5. Decay lifetimes from transient fits of data from the natural sample N2. All measurements were taken at 298 K.

	$\omega(cm^{-1})$	A_1	$\tau_1(ps)$	A_2	$\tau_2(ps)$
GSB	3107	5.6 ($\pm$ 0.2)	0.61 ($\pm$ 0.04)	3.6 ($\pm$ 0.2)	5.9 ($\pm$ 0.3)
ESA$_S$	2963	4.0 ($\pm$ 0.3)	0.54 ($\pm$ 0.06)	3.3 ($\pm$ 0.4)	3.2 ($\pm$ 0.3)
ESA$_B$	3090	3.7 ($\pm$ 0.1)	1.4 ($\pm$ 0.1)	2.6 ($\pm$ 0.1)	8.2 ($\pm$ 0.3)

Transient fits of data taken from N1 at 100 K are compared with the room temperature data in Figure S3.
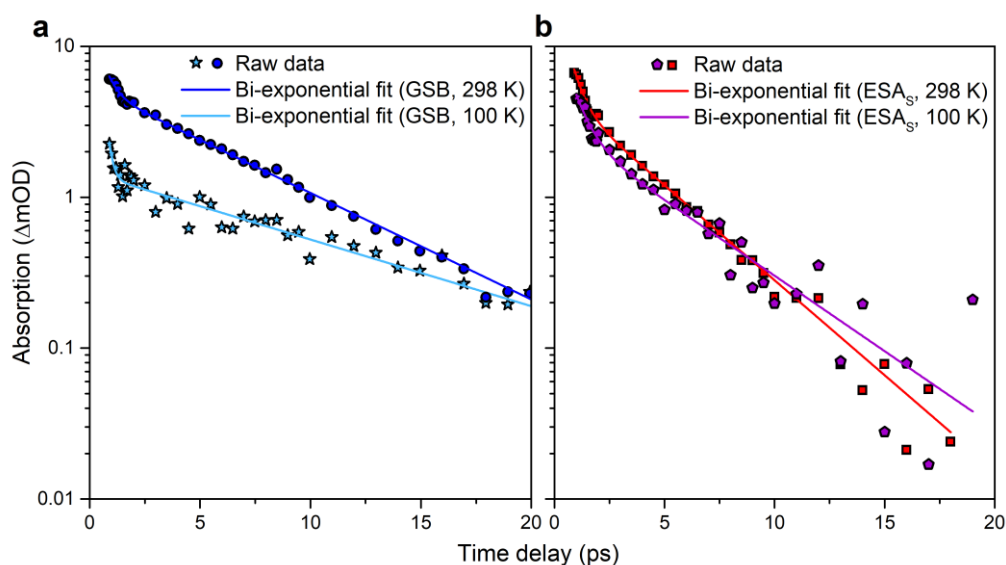

Figure S3. Transient absorption change for N1 at: **a,** peak of GSB, for sample temperatures of 298K (circles) and 100K (stars); **b,** ESA$_S$, 298K (squares) and 100K (pentagons).

To analyse the time- and frequency-dependent transient absorption in more detail, Figure S4 shows the linewidth of the spectra of N1 and S1 at room temperature versus time, while Figure S5 shows the time constants obtained using fits to "slices" of the transient absorption at different wavenumbers.
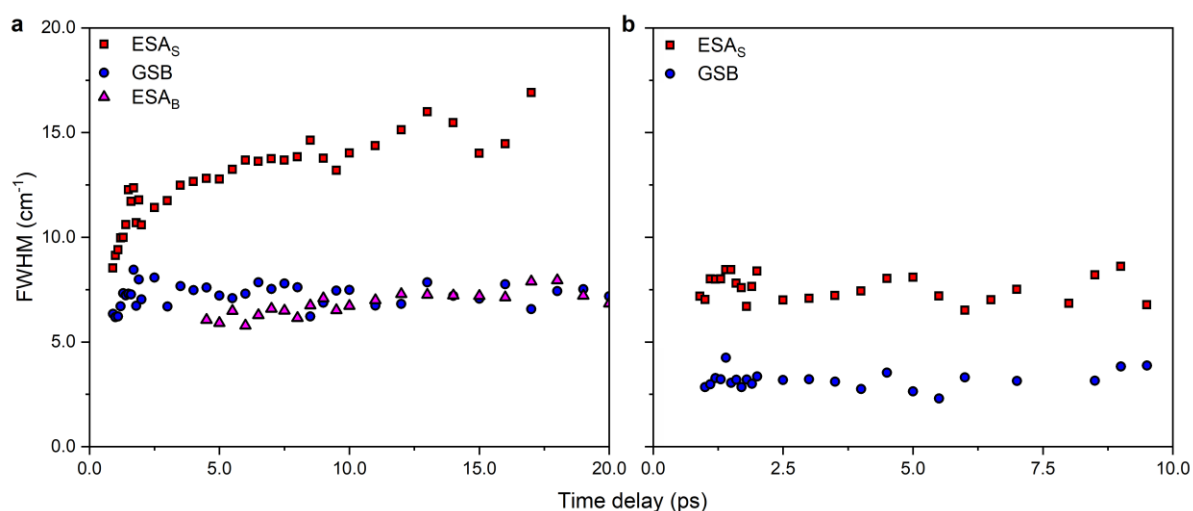
Figure S4. Full-width at half-maximum (FWHM) of the GSB (circles), ESA$_S$ (squares) and ESA$_B$ (triangles) features in the transient absorption spectra of **a,** sample N1, and **b,** sample S1, at room temperature. The FWHM of the GSB is independent of time and can be compared with the total linewidth from FTIR spectroscopy (Table S2). For S1, with purely homogeneous broadening, the FWHM of the GSB (~3 cm^{-1}), is comparable to the linewidth in equilibrium (2.1 cm^{-1}). The poorer spectral resolution of the spectrometer used in the transient experiment accounts for the difference. In N1, the GSB is broader than in S1, as a result of inhomogeneous broadening (see Section S9). For both samples the ESA$_S$ feature has a greater linewidth than the GSB, which we speculate reflects the contribution to the linewidth from energy relaxation from the v_{2S} level. This assertion is based on the observation that the expression for the FWHM linewidth, Γ_{ij}, for an optical transition between state i and state j, with respective population decay lifetimes τ_i and τ_j, is $\Gamma_{ij} = \frac{1}{2\pi}\left(\frac{1}{\tau_i} + \frac{1}{\tau_j}\right)$.[SR5] Hence the linewidth for the ESA associated with the $n = 1$ to $n = 2$ vibrational transition is larger than that for the $n = 0$ to $n = 1$ (as the population lifetime for the ground state is infinite). Pure dephasing may also contribute more substantially to the linewidth for ESA$_S$.
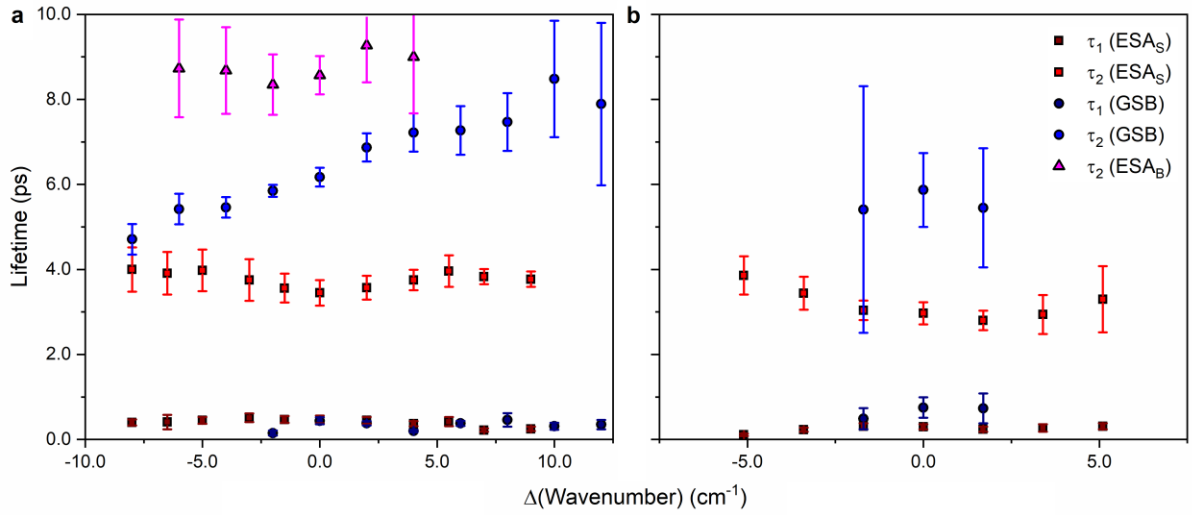
Figure S5. Lifetimes τ_1 and τ_2 obtained from biexponential fits to the transient absorption at different wavenumbers relative to the centers of the GSB, ESA$_S$ and ESA$_B$ features, for: **a,** sample N1 and **b,** sample S1. The dynamics of the GSB, ESA$_S$ and ESA$_B$ are essentially independent of wavenumber. The weak trend in τ_2 for the GSB of sample N1 may indicate subtle changes to the relaxation dynamics for defects in a strained environment but may not be statistically significant given the larger error bars at larger wavenumber difference.

S11. Kinetic model of a 3-level system

To match our energy level system to experimental observations, we created a rate-equation kinetic model that incorporated v_S, v_{2B} and v_0. We defined the populations N_S, N_B and N_0 of each level to change according to the rate equations:

$$\frac{\partial N_S}{\partial t} = -\frac{N_S}{\tau_{S0}} - \frac{N_S}{\tau_{SB}},$$

$$\frac{\partial N_B}{\partial t} = \frac{N_S}{\tau_{SB}} - \frac{N_B}{\tau_{B0}},$$

$$\frac{\partial N_0}{\partial t} = \frac{N_S}{\tau_{S0}} + \frac{N_B}{\tau_{B0}}.$$

We define the following time-constants for decay from one level to another: τ_{S0} for the transition $v_S \to v_0$, τ_{SB} for the transition $v_S \to v_{2B}$ and τ_{B0} for the transition $v_{2B} \to v_0$. We used these equations to determine functions for the decay of the ESAs and recovery of the

GSB, which we fit to the data obtained from diamond N1. To fit the faster component, we added a fixed decay / recovery with a time-constant of 0.4 ps to the functions for the GSB and ESA_S.
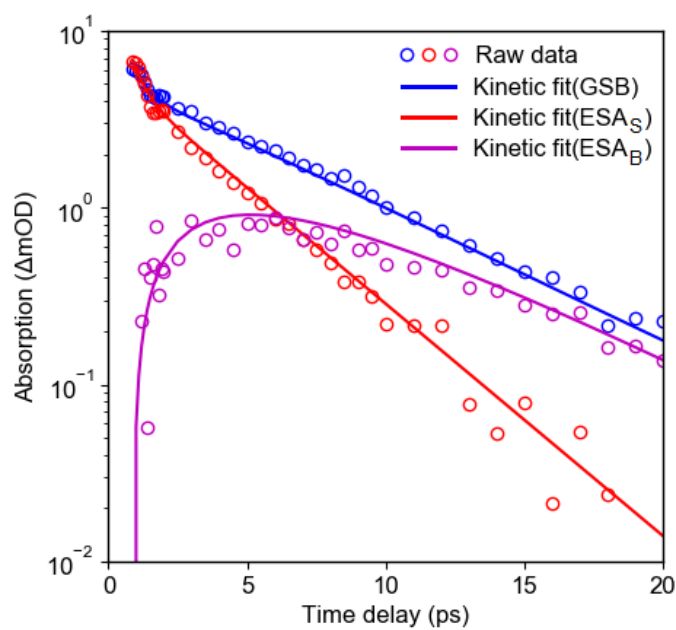

Figure S6. Kinetic fit using data from sample N1 at three different wavelengths corresponding to the maxima of each of the three features GSB, ESA_S and ESA_B. The fit was created from rate equations according to the processes described in Figure 3b in the main paper, and yielded the following time-constants: $\tau_{S0} = 6.9 \pm 0.2$ ps, $\tau_{SB} = 6.4 \pm 0.2$ ps and $\tau_{B0} = 5.6 \pm 0.4$ ps.

Supplemental References (SR)

(SR1) Wilson, E. B.; Decius, J. C.; Cross, P. C. *Molecular vibrations : the theory of infrared and Raman vibrational spectra*; Dover Publications: USA, 2003.

(SR2) Iakoubovskii, K.; Adriaenssens, G. J. Optical characterization of natural Argyle diamonds. *Diam. Relat. Mater.* **2002**, *11*, 125–131.

(SR3)   Maciejewski, A.; Naskrecki, R.; Lorenc, M.; Ziolek, M.; Karolczak, J.; Kubicki, J.; Matysiak, M.; Szymanski, M. Transient absorption experimental set-up with femtosecond time resolution. Femto- and picosecond study of DCM molecule in cyclohexane and methanol solution. *J. Mol. Struct.* **2000**, *555*, 1-13.

(SR4)   Edmonds, A. M.; D'Haenens-Johansson, U. F. S.; Cruddace, R. J.; Newton, M. E.; Fu, K. M. C.; Santori, C.; Beausoleil, R. G.; Twitchen, D. J.; Markham, M. L. Production of oriented nitrogen-vacancy color centers in synthetic diamond. *Phys. Rev. B* **2012**, *86*, 035201.

(SR5)   Rosencher, E.; Vinter, B. *Optoelectronics*; Cambridge University Press: Cambridge, UK, 2002.

(SR6)   Khan, R. U. A.; Martineau, P. M.; Cann, B. L.; Newton, M. E.; Twitchen, D. J. Charge transfer effects, thermo and photochromism in single crystal CVD synthetic diamond. *J. Phys. Condens. Matter* **2009**, *21*, 364214.